RESEARCH ARTICLE

Wind Load Characterization Considering Three Container Cranes in Array Arrangement

DAZHI HUANG[1], YUSHENG SU[2], QING WANG[1], ZETAN GU[1], JIAQI CHENG[1], AND ZHIYU WEI[1]

[1]Faculty of Ocean Engineering, Jiangsu Ocean University, Lianyungang 222005, China
[2]Faculty of Mechanical Engineering, Jiangsu Ocean University, Lianyungang 222005, China

Corresponding author: Yusheng Su (2022210510@jou.edu.cn)

ABSTRACT This study focuses on the wind characteristics of three container cranes discharged side-by-side under wind loads. Three-dimensional models of the three container cranes were established using Computational Fluid Dynamics (CFD). The wind load pattern among the three container cranes was studied by adjusting parameters such as the positional state of the arm of the container cranes, the wind angle, and the spacing of the container cranes. The results show that the maximum wind load borne by container cranes occurs at a 45° wind angle. At a wind angle of 90°, the wind resistance effect was optimal when the spacing between the three container cranes was 45 m. Wind reduction was approximately 63% in the boom-up state of the container cranes and 58% in the boom-down state of the arm. In addition, the study found that the critical spacing of the container cranes was 75 m in the boom-down state of the arm. When the distance between container cranes was greater than 75 m, the wind resistance effect between the container cranes gradually decreased until it disappeared. In the boom-up state of the arm, the critical spacing of the container cranes is 60 m. When the spacing between container cranes was greater than 60 m, the change in the wind resistance coefficient decreased.

INDEX TERMS Container crane, CFD, computational domain, wind angle, wind coefficient, velocity cloud diagram.

I. INTRODUCTION

Container cranes are primarily used for loading and unloading containerized goods and play a key role in connecting water and land cargo transportation [1]. With the rapid development of international trade and increasing demand for imported and exported goods, the stability and performance requirements for container cranes are increasing. In recent years, frequent accidents involving container cranes in ports have caused serious casualties and equipment damage, resulting in significant economic losses in port operations and cargo transportation [2]. Therefore, an in-depth study of the wind load characteristics of container cranes to improve their wind resistance and stability is of great significance for ensuring the safety of port operations [3]. In this study,

The associate editor coordinating the review of this manuscript and approving it for publication was Agustin Leobardo Herrera-May.

we focused on container cranes to investigate their wind load characteristics and effects [4].

Numerous researchers and scholars have studied the wind load characteristics of container cranes under wind loads. Tomczyk et al. [5] discussed a crane control system with a state simulator, load operation, and positioning problems under different wind disturbances; the main components of the dynamical model with a state simulator; methods of wind disturbance compensation; and the results of simulation experiments. Liu et al. [6] combined a shore container crane with a finite element calculation tool to perform a computational fluid dynamics simulation and analysis of the wind load to derive the numerical wind tunnel simulation value of the bridge crane and compared it with the calculated value of computer-aided engineering analysis to obtain a more reasonable numerical simulation method. Gur et al. [7] investigated how various parameters, such as jib position,

yaw angle, asymptotic height, and asymptotic wind speed, affect the failure susceptibility of cranes using commercial software modeling that considers both material and geometric nonlinearities. The stochastic wind field was modeled as a smooth process using a power spectrum combined with a spectral representation of the downwind and crosswind coherence functions. Subsequently, a nonlinear time-course analysis was performed, and the responses in the cases of smooth and unsteady wind fields were compared to provide a reference for understanding the crane vulnerability. Huang [8] discussed the problem of wind loads on tower cranes under non-operating conditions and explored the wind resistance and safety of tower crane structures through experiments and analyses. The results of this study show that when designing and checking a tower crane, its shape should be considered to be significantly affected by transverse winds, its sudden change in mass, and its susceptibility to forced resonance to improve its wind resistance and intrinsic safety of the tower crane. These studies mainly focused on the wind load and static wind vibration response of isolated container cranes, without special consideration of the wind field characteristics. In an actual situation, ports often discharge multiple container cranes side-by-side, compared with a single container crane, and multiple container cranes are more complex owing to the wind load. Fulian et al. [9] studied the flow field characteristics of gantry cranes under a full wind angle, and pointed out the shortcomings of the Crane Design Code in the calculation of the wind load [10]. However, this study analyzed only a single gantry crane and did not consider interference between multiple gantry cranes. Zhang et al. [11] studied the shading effect of four container cranes at multiple wind angles and concluded that the wind-shielding effect between container cranes was consistent. However, they set the distance between two neighboring container cranes to 28 m, and did not consider other distances, which is a certain distance from actual working conditions. Zhu et al. [12] investigated the performance of two typical large container cranes under seismic action. The two cranes were structurally modeled, and nonlinear time-course analysis was used to simulate the structural response under seismic action. The seismic performances of the cranes were evaluated by comparing their responses to different seismic intensities. The study also considered the difference in the response of the cranes at rest and during operation and analyzed the effects of different seismic intensities on the cranes. Wang et al. [13] investigated the bypassing of a single rectangular box girder section under a high Reynolds number; however, their study only analyzed the two-dimensional flow field without simulating the real effect of the three-dimensional wind field.

Most current studies on the wind loads on container cranes have focused on analyzing single or local components [14], [15], [16], [17]. However, in an actual port environment, container cranes are usually placed side-by-side, and to cooperate with the loading and unloading of ships, there is a certain distance between the two neighboring container cranes. This layout of multiple container cranes side-by-side may have a
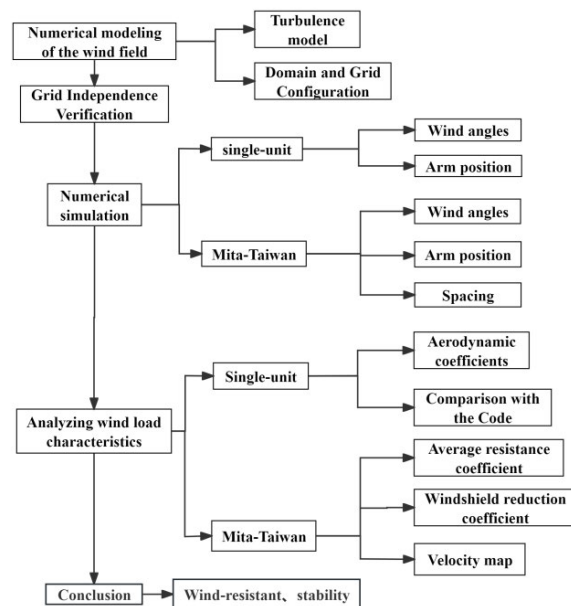

FIGURE 1. Flowchart of the research methodology.

certain impact on the wind conditions of a single container crane. Multiple container cranes at the same time by wind load are more complex, and when three container cranes are arranged side-by-side along the wagon track, they affect each other. The forward position of the container crane may be against the back position of the container crane to produce a certain wind-shielding effect, which is affected by the container crane arm state, wind angle, container crane spacing, and other factors, resulting in a greater difference in the size of the shielding effect. Simultaneously, the container crane in the backward position affected the size of the wake flow to which it was subjected in the forward position. Considering the above complexity, this study aims to investigate the wind load characteristics of container cranes under different wind angles, spacings, and container crane boom parameters through numerical simulations and computational fluid dynamics (CFD) analysis. By setting a single wind speed, the effects of different parameters on wind loads can be better observed and compared. This provided a more accurate understanding of the contribution of each parameter to the wind load and guidance for optimizing the layout of the container crane and improving its wind resistance. Simultaneously, the selection of a single wind speed can simplify the calculation process of the numerical simulation and improve calculation efficiency. The purpose of this study is to gain an in-depth understanding of the wind characteristics of container cranes, provide an accurate reference and guidance for port engineering design, optimize the layout of container cranes, enhance their wind resistance, and improve their performance stability.

Figure 1 shows a flow chart of the research method. The aim of this study is to investigate the wind load characteristics of three container cranes arranged side-by-side through

FIGURE 2. Array of discharging container cranes operating on-site, working together to load and unload containers for the same cargo ship.

(a) boom-up state   (b) boom-down state

FIGURE 3. Container crane model: (a) boom-up state and (b) boom-down state. wind angle for numerical simulation is shown, height of container crane 77.3 m, forward reach 60.3 m, rear reach 75.9 m, total height 77.3 m, gauge 35.5 m, and geographic location of the shore where the container crane is located.

numerical simulation using Computational Fluid Dynamics (CFD). This study was conducted to better understand and optimize the wind loads of three container cranes in a side-by-side arrangement by analyzing the wind loads of a single container crane and those of the container cranes arranged side-by-side. The research method involved obtaining the wind load of a single container crane through aerodynamic data, verifying the accuracy of the numerical simulation by comparing it with the theoretically calculated value, and analyzing the impact of containers by adjusting the wind angle, state of the container crane arm, and spacing, including the wind resistance of the container crane, wind discounting and speed distribution. The theoretical significance of this study lies in its in-depth investigation of the wind characteristics of container cranes to provide an accurate reference and guidance for port engineering design. The practical significance lies in the optimization of the arrangement of container cranes to enhance their wind resistance and performance stability. By studying the wind load characteristics under different spacings and wind angles, more comprehensive data and a deeper understanding can be provided for the assessment and optimization of the wind resistance of container cranes.

II. GUIDELINES FOR MANUSCRIPT PREPARATION

This paper takes the container cranes commonly used in Lianyungang port as an example, its field site container cranes are shown in Figure 2, container cranes are arranged on the shore of the harbor, and can only be moved along the shore along the paved wagon track, so the wind load characteristics of the side-by-side arrangement of container cranes are studied.

Container cranes have two boom states, boom down and boom up. The geometric characteristics of the container crane and its coordinate system are illustrated in Figure 3.

To study the effect of different spacings on the wind load characteristics, by comparing the effect of wind force reduction under different spacings, to derive the effect of wind blocking and wind resistance of cranes under different spacings, to provide more comprehensive data, a more in-depth understanding of the effect of crane spacing on the
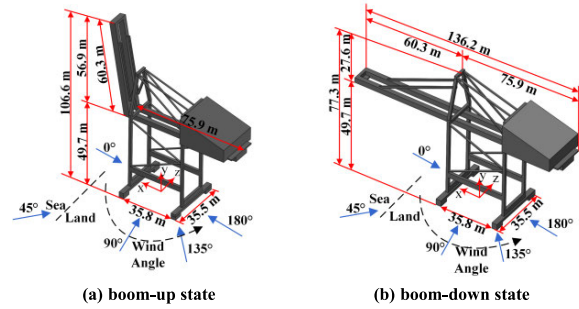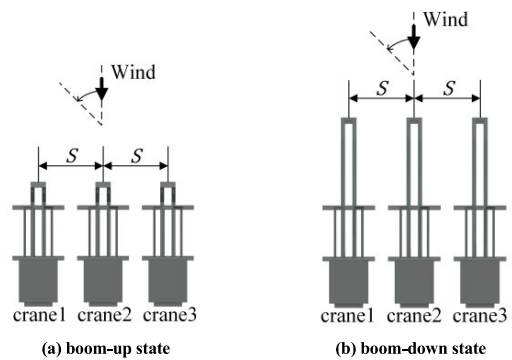

(a) boom-up state   (b) boom-down state

FIGURE 4. Top view of container cranes discharged in an array: (a) boom-up state and (b) boom-down state. In (a), named crane1, crane2, and crane3 from the left to the right, the spacing between the centers of the two container cranes is S, and the orientation of the beginning of the wind angle is for the numerical simulation. The setup in (b) is equivalent to that in (a). To distinguish the container cranes in (a) and (b), the moving arm state of the container cranes is highlighted in the subsequent analysis.

wind load; to optimize the arrangement of cranes and improve their wind resistance, the center spacing was set to 45, 60, 75, and 90 m. Additionally, to comprehensively study the wind load characteristics of container cranes at different wind angles, the wind angle was set to 0°, 45°, 90°, 135°, and 180°, because of the symmetry of the container crane structure, which covers the horizontal angle of the front, diagonal front, side, and diagonal rear, as well as the front and rear. By studying these wind angles, it is possible to obtain a comprehensive understanding of the size and angle changes of the wind loads on container cranes at different angles to better evaluate and optimize the wind resistance of container cranes. The number of container cranes was set along the wind angle as crane1, crane2 and crane3.The top view of the container cranes arranged side-by-side is shown in Figure 4, where S is the spacing between the container cranes.

A. CFD CONFIGURATION

Key numerical modeling considerations required before applying CFD simulations. The selection of the turbulence model, configuration of the domain and mesh, and three key parameters considered central to the CFD numerical

modeling are discussed. In addition, boundary condition settings were used for the CFD simulations.

1) TURBULENCE MODELING

Commonly used turbulence models in Computational Fluid Dynamics (CFD) include Direct Numerical Simulation (DNS), large eddy simulation (LES), and Reynolds averaged Navier-Stokes (RANS). DNS are designed to explicitly resolve the temporal and spatial descent of turbulent motions at all scales down to the smallest dissipation scale and are considered to be the most accurate CFD simulations. However, they are computationally extremely demanding and currently inapplicable for structural engineering purposes. Large eddy simulations have received considerable attention from the Computational Wind Engineering (CWE) community with the recent development of divergence-free inflow turbulence generators [18], [19], [20], [21], and the CWE Application Guide [22]. It has been shown that LES is able to reproduce the results with high accuracy by properly handling the inflow conditions and model parameters [23], [24], [25], [26], [27], [28], [29]. However, to obtain accurate results for problems involving flow separation, the near-wall mesh size must be sufficiently small, which significantly increases computational cost. Thus, LES is still not readily available for general design purposes in industry. Unlike time-dependent DNS and LES, RANS is based on time-averaged Navier-Stokes equations in which time-varying turbulent fluctuations are not explicitly solved. However, they modeled the effect of the averaged flow by making assumptions regarding the eddy viscosity. Owing to their relatively low computational cost, steady-state RANS has been widely studied and has established a good ability to reproduce mean flow characteristics [30], [31]. Researchers have developed various RANS models based on different formulations of Reynolds stresses, which have been calibrated and validated against experimental data for engineering purposes [32], [33]. RANS models have been successfully used in many engineering applications [34], [35], [36], [37]. Considering the requirements for computational efficiency in engineering practice, the relatively low computational cost of the k-ω SST RANS model makes it possible to obtain the prediction results of the flow field around the container crane in a relatively short time, and at the same time, it has good numerical stability, which provides a reliable basis for accurately evaluating the performance of container cranes subjected to wind loads. Therefore, considering the engineering requirements of container cranes and combining the wide applicability, efficient computation, high accuracy, and good stability of the k-ω SST RANS turbulence model, the model has clear advantages for the simulation and analysis of container cranes, and can provide reliable support for engineering design and evaluation.

2) DOMAIN AND GRID CONFIGURATION

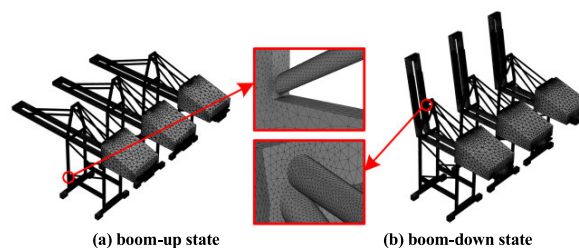Owing to the complex geometry of the model, the computational area was divided into a cylindrical inner field and

FIGURE 5. Container crane model: (a) boom-up state and (b) boom-down state. The grid shown is located in the connection part of the container crane rods, the grid configuration is good, and the subsequent numerical simulation can reflect good accuracy.
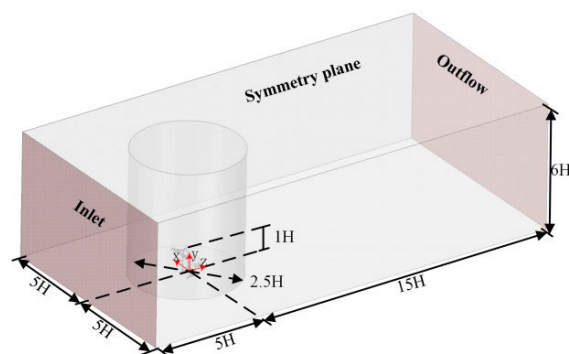

FIGURE 6. Simulated external flow field of entire container crane, inlet, outlet, symmetry plane, and container crane in cylindrical internal flow field.

rectangular outer field. An unstructured tetrahedral mesh was used in the inner region and a structured hexahedral mesh was used for the outer region. The interior mesh was denser to capture the airflow characteristics around the model better. The mesh is merged in the nodes on the surface between the two fields; therefore, the boundary conditions of the surface are set to "internal." The total number of meshes was approximately 14 million, obtained by encrypting the areas around the main and diagonal rods. Only the internal part was changed according to the state, spacing, and state of the arm of the model to solve the wind loads of the grouped container cranes under different conditions. The dimensions and boundary conditions of the computational domain are shown in Figure 5, and are constructed as rectangular boxes.

The computational domain was designed according to the specifications in Figure 6, with a height of 6 H, distance of 5 H from the side of the container crane model to the inlet, and distance of 15 H to the outlet to prevent unexpected flow gradients in the approaching flow profiles [38], [39], and distance of 5 H from the front and rear of the container crane to the sidewalls and top wall of the flow domain, where H denotes the height of the container crane.

The obstruction ratio, defined as the ratio of the projected area of the structure in the inlet plane to the area of the inlet plane of the calculation area, was less than 0.1% for all the building geometries at any wind incidence angle. The domain boundaries were placed sufficiently far away to avoid their influence on airflow around the container

TABLE 1. Grid-independent validation results for single-container cranes.

Error	$\overline{C}_D$	Number of meshes	Meshe	Number of meshes	$\overline{C}_D$	Error
0.69%	0.3837	7038304	M1	5624538	0.3700	0.28%
	0.3810	5677486	M2	3857638	0.3710	
0.09%	0.3807	5045660	M3	3210963	0.3726	0.43%

crane. Symmetric boundary conditions were applied at the top and lateral boundaries of the computational domain to minimize interference effects from these boundaries. Velocity no-slip boundary conditions were applied to building walls and floors. The reason for applying the no-slip wall boundary condition at the bottom is that the wind action creates a natural boundary layer. The distance between the wall and center of the first unit near the wall was defined using the following equation [40]:

$$y^+ = 0.172 \left(\frac{y}{L_{PP}} \right) Re^{0.9} \tag{1}$$

The vertically averaged wind speed and streamwise turbulence intensity were measured by [41], who provided wind-speed profiles using the following equations:

$$U(z) = U_{\text{ref}} \left(\frac{z}{z_{\text{ref}}} \right)^\alpha \tag{2}$$

where $U_{\text{ref}} = 45$ m/s denotes the reference velocity, $z_{\text{ref}} = 10$ m denotes the reference height of the curvature, and $\alpha = 0.11$ denotes the velocity profile index. At the inlet boundary, the turbulent dissipation rate and turbulent kinetic energy distribution are set based on the following equations:

$$\varepsilon(z) = \frac{(u^*)^3}{\kappa(z + z_0)} \tag{3}$$

$$k(z) = \frac{(u^*)^2}{\sqrt{C_\mu}} \tag{4}$$

where $\kappa = 0.41$ is the von Karman constant, $z_0 = 0.0002$ m is the aerodynamic roughness length estimated from the updated Davenport Sea Surface Roughness Classification [42], $C_\mu = 0.09$ is a constant, and u^* is the friction velocity calculated as follows:

$$u^* = \frac{\kappa U(z)}{\ln \left(\frac{z_{\text{ref}} + z_0}{z_0} \right)} \tag{5}$$

B. VERIFICATION OF LATTICE INDEPENDENCE

A wind angle of 90° and the rising and falling of the arm were selected as the single-machine conditions. Wind angles of 45°, 90°, and 135°, an interval of 60 m between the two machines, and the up and down of the arm were selected as the three-machine conditions. Grid convergence studies were conducted for the three different grid sizes. The number of cells used to simulate the single-machine condition and the resistance coefficients for the grid convergence studies are presented in Table 1. The maximum difference in the average drag coefficient was 0.69% between M1 and M2
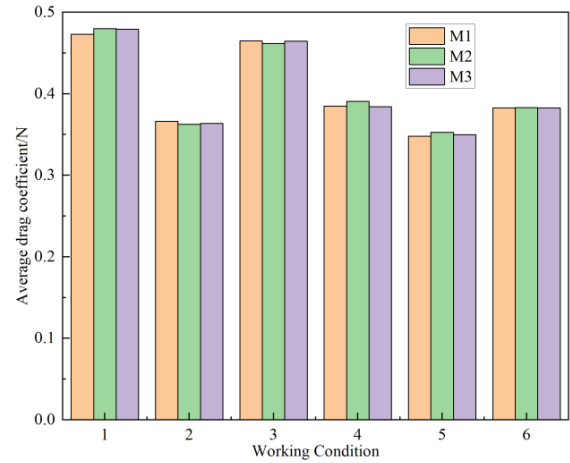

FIGURE 7. Comparison of the simulation performance of three array container cranes under six operating conditions using different grid sizes. M1 was a relatively small grid, M2 was the target grid (the basic grid retained in this study), and M3 was a relatively small grid.

and 0.43% between M2 and M3. Based on the percentage difference obtained, it can be concluded that the average drag coefficient converged. The number of cells used to simulate the three-machine condition and the drag coefficients for the grid-convergence study are shown in Figure 7. Figure 7 shows a comparison of the convergence of the drag coefficients for three grids and six working conditions. The maximum differences in the average percentages between grid calculations M1 and M2 are 1.67%, 1.46%, and 1.45%, respectively. The difference between the M3 and M2 grid calculations was lower. Therefore, the basic grid was retained for the validation study, and M2 was identified as the appropriate grid size for further simulations, considering the difference in the time required for the simulations. Based on the ICEM mesh quality check (the value ranged from 0 to 1; the higher the value, the better the mesh quality), 97.30% of the mesh quality indices were above 0.65, with an average value of 0.91, thereby satisfying the calculation requirements.

III. ANALYSIS AND DISCUSSION

A. SIMULATION OF A SINGLE CONTAINER CRANE

Before studying the wind load characteristics of the three container cranes, it is necessary to analyze the change rule of the aerodynamic coefficient of a single container crane to provide a reference for the subsequent study of three container cranes. The average aerodynamic coefficients of the single-container crane are shown in Figure 8.

In Figure 8: the average drag coefficient $\overline{C}_D$ with the increase of the wind angle, showing "M" type changes. Compared with other wind angles, the average drag coefficients show minimum values at wind angles of 0° and 180°, owing to the relatively small windward area of the container cranes. In 45° and 135° wind angle, the average resistance coefficient of the boom up container cranes, respectively, to achieve the maximum value of 0.48 and 0.47, the boom down container crane average resistance coefficient respectively achieved a
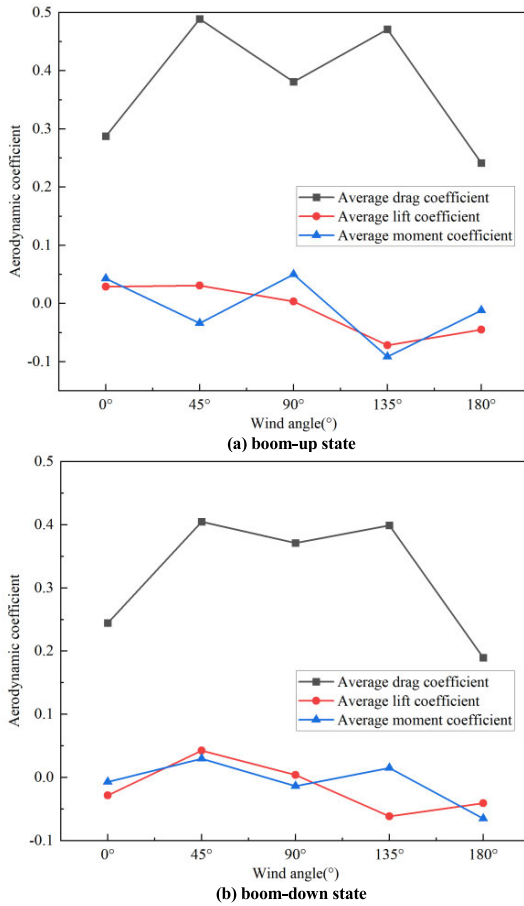
FIGURE 8. Average aerodynamic coefficients of a single container crane: (a) boom-up state and (b) boom-down state. The black target line represents the average drag coefficients, the red represents the average lift coefficient, and the blue represents the average moment coefficient.

FIGURE 9. A comparison of the crane design specification wind load and the simulated wind load is shown: (a) boom-up state and (b) boom-down state. The black target line is the calculated crane design specification wind load and the red line is the calculated numerical simulation wind load.

maximum value of 0.40 and 0.39, indicating that the container crane in the oblique wind angle by the wind resistance is larger; in the 90° wind angle, the average resistance coefficient of the boom-up state container crane 0.38, greater than the average resistance coefficient of the average resistance coefficient of the boom-down state container crane 0.38 container crane 0.37, the overall container crane boom up than the arm to be subjected to a greater resistance to the down; average lift coefficient $\overline{C}_L$ and the average moment coefficient $\overline{C}_M$ have a small range of variation, and their values are located near zero. From the variation range of the aerodynamic coefficients, it can be observed that the drag coefficient of the container crane was much larger than the lift and moment coefficients. This indicates that the wind load suffered by the container cranes was primarily at the angle of incoming flow. Therefore, when analyzing the three container cranes, the wind load on the container crane can be approximated as the average resistance value. In the "Crane Design Code," the angle of the container crane wind load is specified as the most unfavorable angle for container cranes; however, it does not specify a specific wind angle. According to the above analysis, the 45° and 135° wind angles for the container cranes are relative to the unfavorable wind angle.
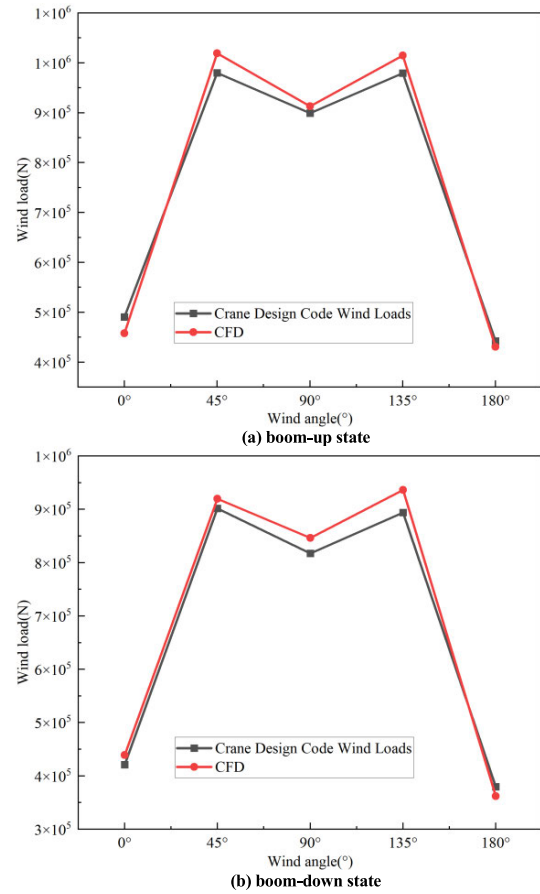
B. COMPARISON OF CODE WIND LOADS WITH SIMULATED VALUES

In the Crane Design Code, wind loads on container cranes are defined as:

$$F = CPA \cdot \sin^2 \theta \tag{6}$$

where F-container crane wind load, N; C-wind carrier type coefficient, dimensionless, take 1.6; P-calculated wind pressure, N/m^2, take 250 N/m^2; θ-wind angle, (°), the value of which changes in the range of 0-180°.

The wind loads of a single container crane at different wind angles were extracted using FLUENT and compared with the calculated values of the Crane Design Code. The comparison between the wind load of the "Crane Design Code" and the simulated wind load is shown in Figure 9.

It can be seen from Figure 9 that the CFD simulation value is slightly higher than the "Crane Design Code," and the change rule of the wind load and the average drag coefficient change rule are consistent. In the boom-up state container crane, the wind load of the simulation and the Code reaches its maximum value under 45° and 135°, and under 0° wind angle, the simulation value is 45.78×10^4 N, and the calculated value of the Code is 49.04×10^4 N, and under 45° wind

angle, the simulation value is 45.78×10^4 N, and the calculated value of the Code is 49.04×10^4 N; in the boom-down state container crane, the wind load of the simulation and the Code reaches its maximum value under 45° and 135°, Under the wind angle of 135°, the simulation value is 93.66×10^4 N, and the calculated value of the Code is 89.41×10^4 N, and under the wind angle of 180°, the simulation value is 36.18×10^4 N, and the calculated value of the Code is 37.98×10^4 N; thus, it can be seen that the relative error between the simulation and the Code is about 6.66% or less, which verifies the accuracy of the above simulation calculations.

C. SIMULATION OF THREE CONTAINER CRANES
1) AVERAGE DRAG COEFFICIENT FOR CONTAINER CRANES
A three-machine numerical simulation was conducted using three influencing factors wind angle, container crane spacing, and arm states to study the wind force coefficient $\overline{C}_D$. A three-machine numerical simulation was performed under 40 operating conditions. The average resistance coefficient of the container crane is shown in Figure. 10.

As show in Figure 10: Crane2 and crane3 there is no masking relationship between the two, and their average resistance coefficients are within the average resistance coefficient of a single container crane near the change point, which is equivalent to that of a single container crane.

At a container crane spacing of 45m, the boom-up and the boom-up in two states, crane1and crane2, between the existence of wind-blocking folding, particularly at a 90° wind angle, were more evident, and the average drag coefficient differences were 63.42% and 58.21%, respectively. crane2The average drag coefficient was slightly larger than that of crane3; However, the difference in the average drag coefficient was only 2%, which was almost equal, indicating a weak wind break.

With an increase in spacing S, the average drag coefficient showed a decreasing trend. However, there was a significant difference in the 90° wind angle, which manifested as a gradual increase in the wind-blocking folding of crane2forcrane3, with an increase in the boom-up state container cranes specifically manifested as 3.90%, 13.95%, 17.74%, and 19.25%, and boom-down state container cranes specifically manifested as 6.93%, 14.07%, 17.29%, and 18.65%. This is due to the fact that the first container crane forms a large obstruction in the airflow, and the air flow through it undergoes a significant reduction in speed and change in direction. This causes the airflow to be disturbed further before it touches the second container crane, thereby creating a stronger wind-blocking effect.

In addition, as the wind angle increases, the average drag coefficients ofcrane1, crane2, and crane3 show an ''M'' trend, but there is a large gap near 90°, indicating that the container cranes are subjected to a wind angle of 90°, and the first container crane can withstand the wind load well, thereby reducing the impact of the wind on the back of the container crane.

2) CONTAINER CRANE WINDBREAK REDUCTION FACTOR
Since the wind load on the container crane is approximately equal to the drag force on the container crane, in order to further account for the wind shading effect of crane1 oncrane2, and the wind shading effect of crane2 oncrane3, the windbreak discount factor η_1 and η_2 are introduced and evaluated. Specify the container crane windbreak discount factor as

$$\eta_1 = \frac{\overline{C_{Dcrane1}} - \overline{C_{Dcrane2}}}{\overline{C_{Dcrane1}}} \tag{7}$$

$$\eta_2 = \frac{\overline{C_{Dcrane2}} - \overline{C_{Dcrane3}}}{\overline{C_{Dcrane2}}} \tag{8}$$

where $C_{Dcrane1}$ denotes the dimensionless first-container crane average resistance coefficient; $C_{Dcrane2}$ denotes the dimensionless second-container crane average resistance coefficient; and $C_{Dcrane3}$ denotes the dimensionless third-container crane average resistance coefficient.

The container crane wind resistance discount factors are listed in Tables 2 and 3. Table 2 shows the crane1-to-crane2 wind-blocking discount coefficients (η_1) and Table 3 shows the crane2-to-crane3 wind-blocking discount coefficients (η_2). As there is almost no blocking relationship between the container crane machines at wing angles of 0° and 180°, the wind-blocking discount factor tends to zero; therefore, the table is not involved.

The results are presented in Tables 2 and 3. The results of the study of single container cranes show that the maximum value of the wind load suffered by container cranes occurs at wind angles of 45° and 135°. The most unfavorable wind angles for the three container cranes were 45° and 135°. At a wind angle of 90°, the first container crane had the most significant blocking effect on the second container crane. In the boom-up state of the container cranes, when the spacing between the container cranes was 45 m, the first container crane had the best wind-blocking effect on the second container crane, with a wind discount of approximately 63%. In the boom-down state of the container cranes, when the spacing between the container cranes was 45 m, the wind-blocking effect was optimal, with approximately 58% wind discounting. These results indicate that container cranes can better resist wind in these cases. A critical spacing exists between the three container cranes. The critical spacing between the first and second container cranes at wing angles of 45°and 135° is 75 m. When the spacing was greater than 75 m, the shading effect of the first container crane weakened gradually. At wind angles of 45° and 135°, the critical spacing from the second container crane to the third container crane was 45 m. However, the change in the wind-blocking discount coefficient decreased, and the shielding effect of the second container crane to the third container crane gradually increased. The maximum wind blocking discount coefficients of the up and down states of the boom are 0.63 and 0.58, respectively. This implies that, under these state conditions, the container crane can reduce the wind load by approximately 60%.
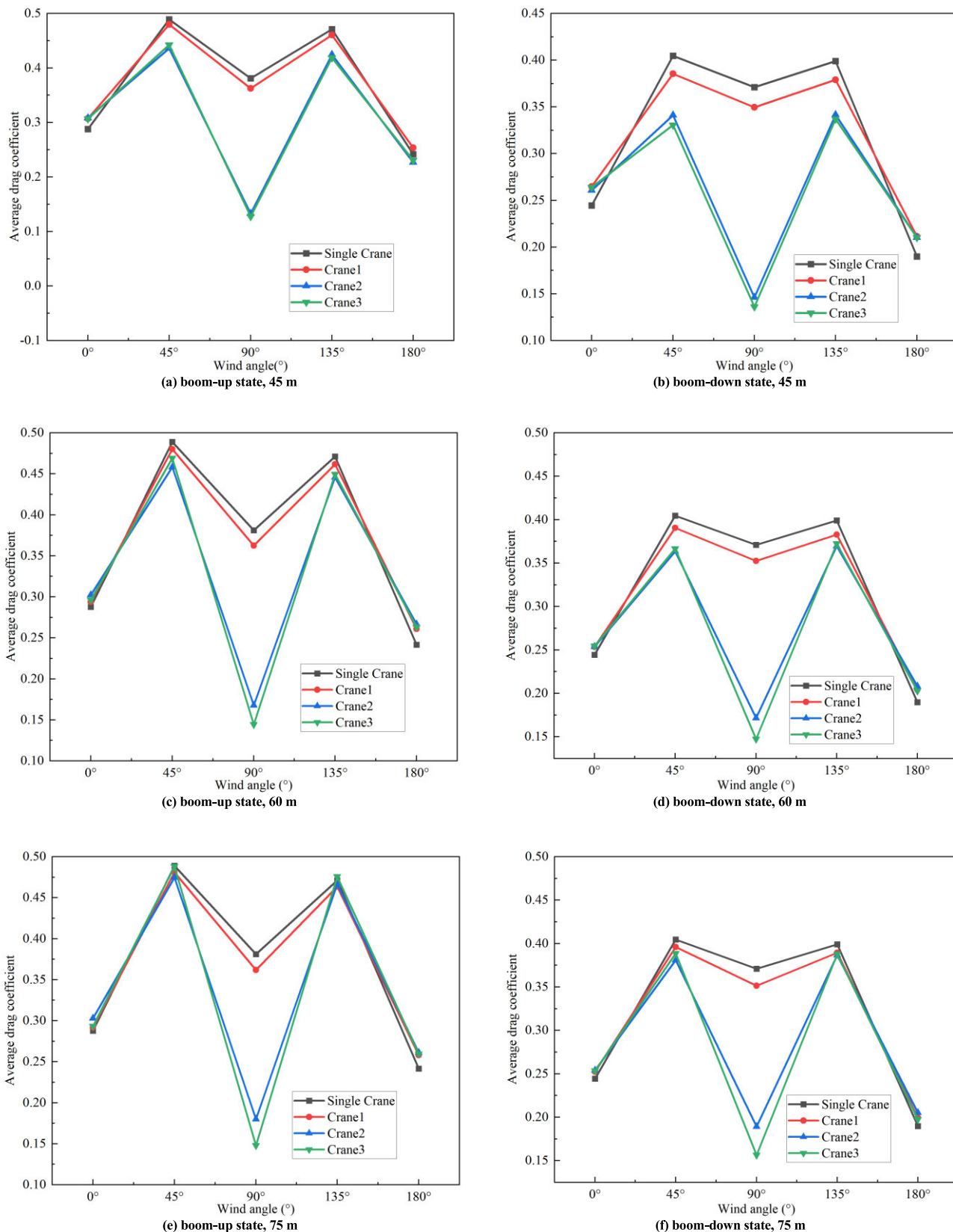
FIGURE 10. The average resistance coefficients of the container cranes are as follows: (a) boom-up state and (b) boom-down state. In each figure, the average drag coefficients for a single crane simulation and the average drag coefficients for crane1, crane2 and crane3 in the array of three cranes are shown.

FIGURE 10. *(Continued.)* The average resistance coefficients of the container cranes are as follows: (a) boom-up state and (b) boom-down state. In each figure, the average drag coefficients for a single crane simulation and the average drag coefficients for crane1, crane2 and crane3 in the array of three cranes are shown.
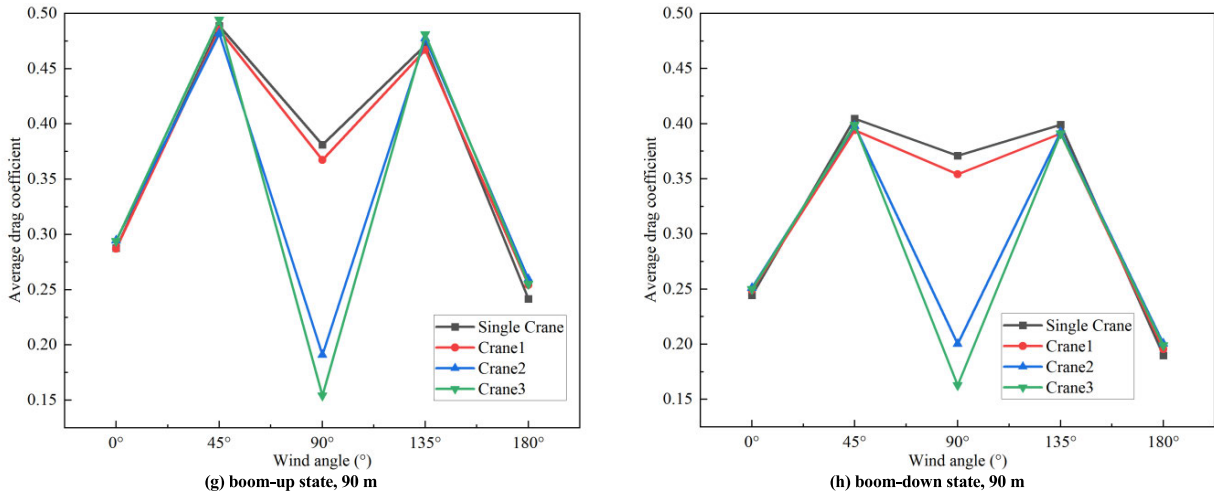
TABLE 2. Container crane machine windshield reduction factor (η_1).

Container crane spacing (S/m) (boom-up state)	Wind angle (°) (boom-up state)			Wind angle (°) (boom-down state)			Container crane spacing (S/m) (boom-down state)
	45	90	135	45	90	135	
45	0.09	0.63	0.08	0.12	0.58	0.10	45
60	0.05	0.54	0.03	0.07	0.51	0.03	60
75	0.01	0.50	-0.01	0.04	0.46	0.01	75
90	0.01	0.48	-0.02	-0.01	0.43	-0.01	90

TABLE 3. Container crane machine windshield reduction factor (η_2).

Container crane spacing (S/m) (boom-up state)	Wind angle (°) (boom-up state)			Wind angle (°) (boom-down state)			Container crane spacing (S/m) (boom-down state)
	45	90	135	45	90	135	
45	-0.01	0.04	0.01	0.03	0.07	0.01	45
60	-0.02	0.14	-0.01	-0.01	0.14	0	60
75	-0.02	0.18	-0.02	-0.02	0.17	0	75
90	-0.02	0.19	-0.01	-0.01	0.19	0	90

3) VELOCITY CHANGE CLOUD MAPS

To further explain the interaction between the three container cranes arranged in groups, it is necessary to analyze the change rule of the flow field under the two-container crane arm states, S = 45, 60, 75, and 90 m, and wind angles of 45°, 90°, and 135°. Figures 11 and 12 illustrate the contour plots of the horizontal wind speed for the two states of the container cranes arranged in groups. A horizontal height of 50 m was chosen for the slicing plane to demonstrate the velocity-wave flow around the arm and plant. The velocity clouds of the upper slicing plane of the container cranes at different wind angles are shown in Figures 11 and 12.

As can be seen from Figure 11: with the increase of the distance S, the airflow velocity between the three container cranes gradually increases, the speed reduction effect is weakened; when the wind angle of 45°, the speed of the flow in the first container crane main beam and the corner of the plant separation to the second container crane, when S = 75 m, only a small portion of the airflow will be along the movement of the to the rear end of the 's tail end, container crane upper assembly around the air velocity with the increase in wind angle shows a "first increase and then decrease" trend; when S = 90 m's tail flow is almost no effect to, on shading effect disappears, the airflow velocity between container cranes and the entrance velocity is approximately equal; when the wind angle of 135°, the folding effect is mainly embodied in the state of the arm, on the most obvious reduction of the velocity flow when the S = 75 m, due to the three container cranes spaced farther apart, making the air-flow velocity between the three container cranes appear negative; when the wind angle of 90°, the wind blocking folding effect is most obvious, the main blocking parts in the
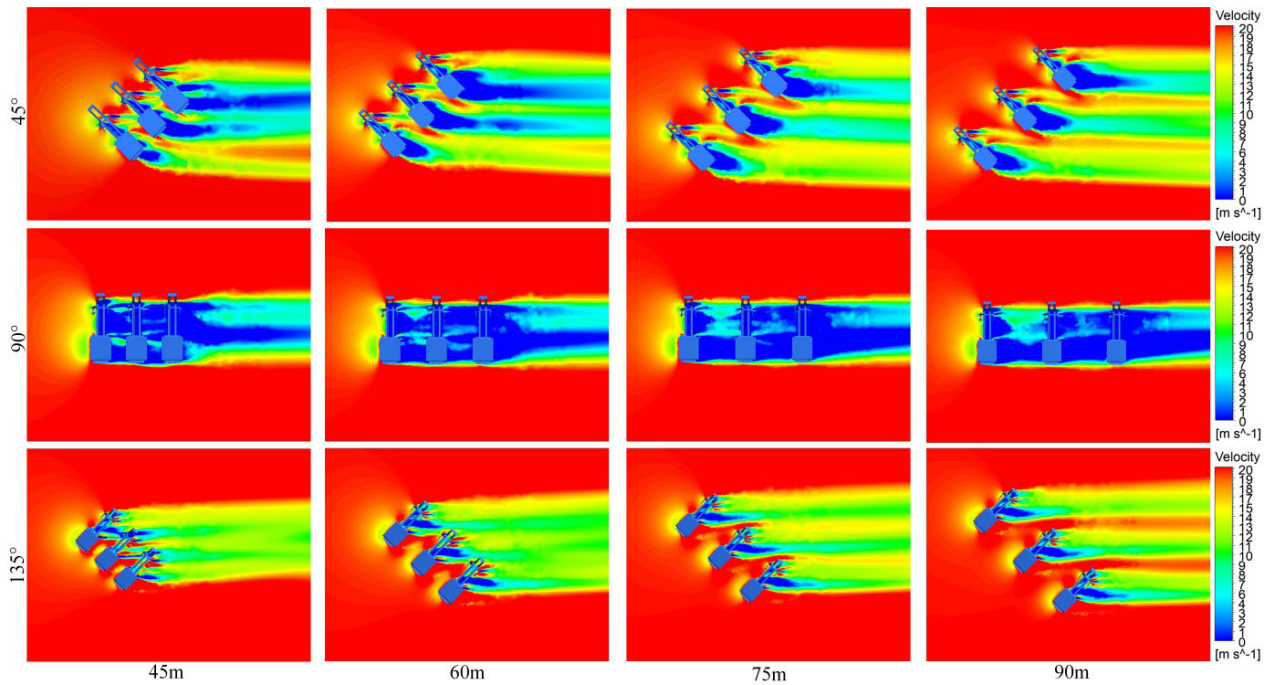
FIGURE 11. Interception of three arrays of container cranes horizontal height of 50 m slicing plane, in different wind angles, different container crane spacings, and container crane boom-up state slicing plane velocity clouds. Each row had the same wind angle angles of 45°, 90°, and 135°. Each row had the same container crane spacing of 45 m, 60 m, 75 m, 90 m.

FIGURE 12. Interception of three arrays of container cranes horizontal height of 50 m slicing plane, in different wind angles, different container crane spacings, and container crane boom-down state the slicing plane velocity cloud. Each row has the same wind angle angles of 45°, 90°, and 135°. Each row had the same container crane spacing of 45 m, 60 m, 75 m, 90 m.
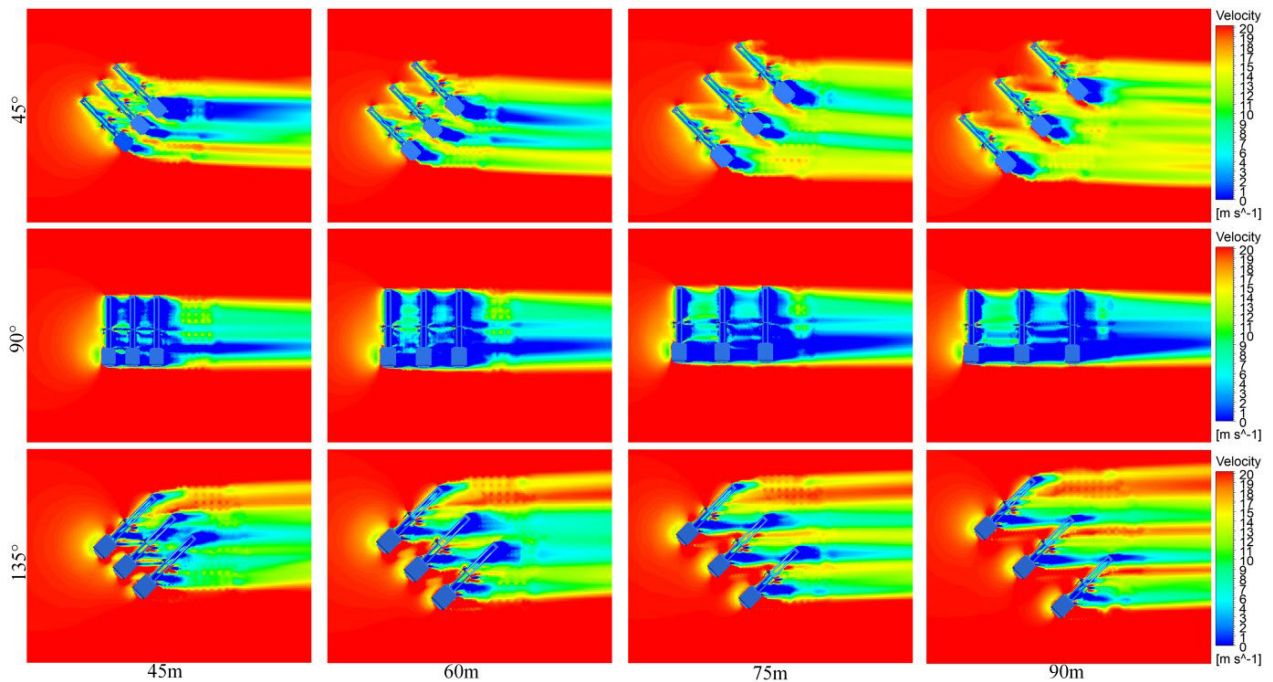
land-side beams, plant and sea-side columns, as the distance increases, the velocity flow to amplify wind loads.

As shown in Figure 12, the airflow velocity between the three container cranes decreased gradually with increasing spacing S, and the velocity discounting effect increased. More windward components are sheltered when the crane arm is in a boom-down state than when it is in at boom-up state. Although the wake may enhance turbulence, the shading

effect always dominates and tends to reduce wind load. For the container crane with a wind angle of 135°, the shielding effect of the wake was evident and the velocity flow amplified the wind load.

IV. CONCLUSION

The scientific contributions of this study are as follows: 1. Analysis of wind load characteristics of container cranes: This study analyzes the wind load characteristics of container cranes through numerical simulation and thoroughly researches the wind resistance of container cranes. This provides an accurate reference and guidance for port engineering design, which helps optimize the layout and parameters of container cranes, improve their wind resistance, reduce the probability of accidents, and ensure the safety of port operations. 2. Application of CFD simulation: This study adopted a computational fluid dynamics (CFD) simulation method. The method has wide applicability, high computational efficiency, high accuracy, and good stability in engineering practice and provides reliable support for engineering design and evaluation. 3. Container crane layout optimization: This study investigated the influence of the container crane layout on the wind-blocking effect by analyzing the layout of container cranes at different spacings and wind angles. The results showed that at a specific spacing and wind angle, container cranes could better withstand the wind and reduce the wind load by approximately 60%. This is important for optimizing the wind load situation when multiple container cranes are arranged side-by-side. In summary, this study conducted an in-depth study on the wind characteristics of multiple container cranes, revealing the wind-blocking effect and critical spacing of container cranes and providing an accurate reference and guidance for port engineering design. This is of great practical significance for improving the wind resistance and stability of container cranes, reducing the probability of accidents, and ensuring port operation safety.

REFERENCES

[1] D.-S. Han and G.-J. Han, "Force coefficient at each support point of a container crane according to the wind direction," *Int. J. Precis. Eng. Manuf.*, vol. 12, no. 6, pp. 1059–1064, Dec. 2011.

[2] S.-K. Li, J.-Y. Lei, and Y.-G. Yang, "Research on wind load characteristics of tower crane based on segmental model force measurement method," *J. Railway Sci. Eng.*, pp. 1–12, 2024.

[3] W. Chen, X. Qin, Z. Yang, and P. Zhan, "Wind-induced tower crane vibration and safety evaluation," *J. Low Freq. Noise, Vib. Act. Control*, vol. 39, no. 2, pp. 297–312, Jun. 2020.

[4] S. W. Lee, T. W. Ahn, D. S. Han, T. H. Kim, and G. J. Han, "The structural stability analysis of a container crane according to the boom shape using wind tunnel test," *Key Eng. Mater.*, vol. 347, pp. 365–372, Sep. 2007.

[5] J. Tomczyk, J. Cink, and A. Kosucki, "Dynamics of an overhead crane under a wind disturbance condition," *Autom. Construct.*, vol. 42, pp. 100–111, Jun. 2014.

[6] C.-Y. Liu, Q. Liu, and L. Luo, "Numerical wind tunnel analysis of shore-side container cranes," *Port Handling*, no. 1, pp. 7–11, 2024.

[7] S. Gur and S. Ray-Chaudhuri, "Vulnerability assessment of container cranes under stochastic wind loading," *Struct. Infrastruct. Eng.*, vol. 10, no. 12, pp. 1511–1530, Dec. 2014.

[8] S.-X. Huang, "Discussion on wind load of tower crane in non-operating condition based on wind vibration theory," *China Special Equip. Saf.*, vol. 40, no. 1, pp. 34–39, 2024.

[9] F.-L. Zang, W.-M. Cheng, and R. Du, "Analysis of wind load response of large gantry crane under full wind angle," *Comput. Simul.*, vol. 39, no. 3, pp. 303–307, 2022.

[10] *Crane Design Code*, China Standard Publishing House, Beijing, China, 2008.

[11] Y.-H. Zhang, H.-J. Gu, and S. Lu, "Research on wind load calculation of container crane transportation ship," *Chin. Shipbuilding*, vol. 62, no. 2, pp. 255–266, 2021.

[12] X.-H. Zhu, W.-M. Cheng, and J.-B. Shao, "Research on wind vibration characteristics of large gantry cranes," *Mech. Design Manuf.*, no. 9, pp. 63–66, 2013.

[13] S.-B. Wang, W.-M. Cheng, R. Du, Y.-P. Wang, and Y. Deng, "Aerodynamic characteristics of rectangular section at ultra high Reynolds number," *J. Appl. Mech.*, vol. 37, no. 5, pp. 1907–1914, 2020.

[14] M. Moeini, N. Brown, and A. M. Memari, "Estimating hurricane-induced vertical surge and wave loads on elevated coastal buildings based on CFD simulations and ensemble learning," *Coastal Eng.*, vol. 183, Aug. 2023, Art. no. 104325.

[15] M. H. Dao, B. Zhang, X. Xing, J. Lou, W. S. Tan, Y. Cui, and B. C. Khoo, "Wind tunnel and CFD studies of wind loadings on topsides of offshore structures," *Ocean Eng.*, vol. 285, Oct. 2023, Art. no. 115310.

[16] H. Kataoka, Y. Ono, and K. Enoki, "Applications and prospects of CFD for wind engineering fields," *J. Wind Eng. Ind. Aerodyn.*, vol. 205, Oct. 2020, Art. no. 104310.

[17] D. Gemayel, M. Abdelwahab, T. Ghazal, and H. Aboshosha, "Modelling of vertical axis wind turbine using large eddy simulations," *Results Eng.*, vol. 18, Jun. 2023, Art. no. 101226.

[18] Y. Ito and K. Sasaki, "Effect of modelled areas and inflow turbulence on the wind characteristics over a densely built-up city," *J. Wind Eng. Ind. Aerodyn.*, vol. 245, Feb. 2024, Art. no. 105646.

[19] H. R. Karimi and N. Shabakhty, "Evaluation of wind-induced turbulence around offshore platforms in different wind speeds and directions, along with safety assessment of helicopter operation and helideck's air-gap optimization," *Results Eng.*, vol. 21, Mar. 2024, Art. no. 101950.

[20] M. H. Aksoy, "Flow characteristics and passive flow control of circular cylinders with triangular vortex generators: An experimental investigation," *Appl. Ocean Res.*, vol. 142, Jan. 2024, Art. no. 103836.

[21] L. Cotteleer, R. Longo, F. Debaste, and A. Parente, "Flow-based stress-blended eddy simulation: A local RANS/LES turbulence model for urban flow CFD simulations," *Results Eng.*, vol. 21, Mar. 2024, Art. no. 101679.

[22] M. S. Thordal, J. C. Bennetsen, S. Capra, and H. H. H. Koss, "Towards a standard CFD setup for wind load assessment of high-rise buildings: Part 1—Benchmark of the CAARC building," *J. Wind Eng. Ind. Aerodyn.*, vol. 205, Oct. 2020, Art. no. 104283.

[23] M. Ghasemnezhad and E. Roohi, "Large eddy simulation of cavitating flow around a pitching hydrofoil," *Ocean Eng.*, vol. 292, Jan. 2024, Art. no. 116547.

[24] L. Zhou, T. Gao, Y. Wang, J. Wang, J. Gong, and J. Li, "Large eddy simulation of enhanced heat transfer in grooved channel with pulsating flow corresponding to hydrodynamic frequency," *Int. J. Heat Mass Transf.*, vol. 218, Jan. 2024, Art. no. 124822.

[25] Y. Liu, J. Liu, X. Li, Z. Li, G. Li, and L. Zhou, "Large eddy simulation of particle hydrodynamic characteristics in a dense gas-particle bubbling fluidized bed," *Powder Technol.*, vol. 433, Jan. 2024, Art. no. 119285.

[26] B. De, A. Kumar, and S. K. Mishra, "Large eddy simulation of wind loading on an anticlastic conical tensile membrane," *J. Wind Eng. Ind. Aerodyn.*, vol. 246, Mar. 2024, Art. no. 105658.

[27] T. Gui, G. Ou, L. Guo, and Z. Ge, "Large eddy simulation on heat transfer characteristics of supercritical water in double-pipe heat exchanger," *Int. J. Thermal Sci.*, vol. 195, Jan. 2024, Art. no. 108660.

[28] L. Tang, H. Liu, C. Zheng, and Y. Luo, "A new probability-distribution scale synthetic eddy method for large eddy simulation of wind loads," *J. Wind Eng. Ind. Aerodyn.*, vol. 249, Jun. 2024, Art. no. 105732.

[29] A. C. W. Creech and A. Jackson, "Time-series data from a hybrid finite element large eddy simulation of flow over a backward-facing step," *Data Brief*, vol. 54, Jun. 2024, Art. no. 110330.

[30] L. Tian, Y. Song, Z. Wang, N. Zhao, C. Zhu, and X. Lu, "Predictive capability of an improved AD/RANS method for multiple wind turbines and wind farm wakes," *Energy*, vol. 297, Jun. 2024, Art. no. 131207.

[31] H. Iddou, N. N. Bouda, and K. Zereg, "Computational fluid dynamics study on the efficiency of straight-bladed vertical axis wind turbine," *Int. J. Thermofluids*, vol. 22, May 2024, Art. no. 100672.

[32] J. Abeken, D. de Zélicourt, and V. Kurtcuoglu, "Incorporating unresolved stresses in blood damage modeling: Energy dissipation more accurate than Reynolds stress formulation," *IEEE Trans. Biomed. Eng.*, vol. 71, no. 2, pp. 563–573, Feb. 2024.

[33] X. Fu, S. Fu, C. Liu, M. Zhang, and Q. Hu, "Data-driven approach for modeling Reynolds stress tensor with invariance preservation," *Comput. Fluids*, vol. 274, Apr. 2024, Art. no. 106215.

[34] S. K. Raghunathan Srikumar, L. Cotteleer, G. Mosca, A. Gambale, and A. Parente, "Application of a comprehensive atmospheric boundary layer model to a realistic urban-scale wind simulation," *Building Environ.*, vol. 253, Apr. 2024, Art. no. 111330.

[35] F. Alavi, A. A. Moosavi, A. Sameni, and M. Nematollahi, "Numerical simulation of wind flow characteristics over a large-scale complex terrain: A computational fluid dynamics (CFD) approach," *City Environ. Interact.*, vol. 22, Apr. 2024, Art. no. 100142.

[36] Y. Masoumi, F. Taheri-Behrooz, and S. M. Hasheminejad, "Numerical study of a synergistic hybrid energy harvesting system for bladeless wind turbines," *Energy Convers. Manage.*, vol. 307, May 2024, Art. no. 118342.

[37] J. J. Peñaloza-Gutierrez, A. E. Tejada-Martínez, and M. C. Boufadel, "Reynolds-averaged Navier–Stokes simulation of nearshore Langmuir circulation and the formation of oil-particle aggregates," *Ocean Model.*, vol. 187, Feb. 2024, Art. no. 102306.

[38] K. Wijesooriya, D. Mohotti, C.-K. Lee, and P. Mendis, "A technical review of computational fluid dynamics (CFD) applications on wind design of tall buildings and structures: Past, present and future," *J. Building Eng.*, vol. 74, Sep. 2023, Art. no. 106828.

[39] J. Zhang, C. Zhu, and C. Ma, "Driving safety analysis of wind–vehicle–bridge system considering aerodynamic interference," *J. Wind Eng. Ind. Aerodyn.*, vol. 245, Feb. 2024, Art. no. 105649.

[40] R. Deng, D.-B. Huang, G.-L. Zhou, and H.-W. Sun, "Exploration of some CFD factors affecting ship resistance calculation," *Ship Mech.*, vol. 17, no. 6, pp. 616–624, 2013.

[41] I. M. V. Andersen, "Wind loads on post-panamax container ship," *Ocean Eng.*, vol. 58, pp. 115–134, Jan. 2013.

[42] J. Wieringa, "Updating the davenport roughness classification," *J. Wind Eng. Ind. Aerodyn.*, vol. 41, nos. 1–3, pp. 357–368, Oct. 1992.

YUSHENG SU was born in Xuzhou, Jiangsu, China, in 1999. He received the B.E. degree in electrical engineering and automation from the Gongqing College, Nanchang University, Jiujiang, China, in 2022. He is currently pursuing the M.S. degree with the School of Mechanical Engineering, Jiangsu Ocean University.

His research interests include the health inspection and forecasting of port equipment.

QING WANG was born in Xuzhou, Jiangsu, China, in 1999. She received the B.E. degree from the School of Mechanical Engineering, Jiangsu Ocean University, China, in 2021. She is currently pursuing the M.S. degree with the School of Marine Engineering, Jiangsu Ocean University.

Her research interest includes the structural health monitoring of ships.

ZETAN GU was born in Huaian, Jiangsu, China, in 2000. He received the B.E. degree in mechanical design and manufacturing and automation from Jiangsu Ocean University, in 2018, where he is currently pursuing the M.S. degree in marine engineering.

His research interests include marine intelligent equipment and health inspection technology.

DAZHI HUANG was born in Xinye, Henan, China, in 1977. He received the B.E. degree in mechanical and electrical engineering from Shenyang University of Technology and Northeastern University, Shenyang, China, in 1999, the M.E. degree in mechanical and electrical engineering from Northeastern University, Shenyang, in 2003, and the Ph.D. degree in mechanical engineering and automation from Nanjing University of Aeronautics and Astronautics, Nanjing, China, in 2018.

From 2004 to 2019, he was an Associate Professor and the Department Head with the College of Mechanical and Ocean Engineering, Huaihai Institute of Technology, Huaihai, China. From 2019 to 2020, he was an Associate Professor and the Associate Dean with the College of Mechanical and Ocean Engineering, Ocean University of Jiangsu, China. Since 2020, he has been a Professor and the Associate Dean with the College of Ocean Engineering, Ocean University of Jiangsu, China. He has authored more than 30 articles and 11 inventions. His research interests include the health detection and forecasting of port equipment.

JIAQI CHENG was born in Nanjing, Jiangsu, China, in 2000. He received the B.E. degree in electrical engineering and automation from Zijin College, Nanjing University of Science and Technology, Nanjing, in 2023. He is currently pursuing the M.S. degree with the School of Ocean Engineering, Jiangsu Ocean University.

His research interests include health detection and forecasting of port equipment.

ZHIYU WEI was born in Xuzhou, Jiangsu, China, in 2000. He received the B.E. degree in mechanical design and manufacturing and automation from the College of Automotive and Mechanical Engineering, Changchun College of Engineering, Changchun, China, in 2023. He is currently pursuing the M.Sc. degree with the College of Marine Engineering, Jiangsu Ocean University.

His research interests include health inspection and forecasting of harbor equipment.

• • •